

Banner appropriate to article type will appear here in typeset article

Numerical simulations of attachment-line boundary layer in hypersonic flow, Part II: the features of three-dimensional turbulent boundary layer

Youcheng, Xi¹ †, Bowen, Yan², Guangwen Yang² and Song, Fu¹

¹School of Aerospace Engineering, Tsinghua University, 100084 Beijing, China

²Institute of High Performance Computing, Department of Computer Science and Technology, Tsinghua University, 100084 Beijing, China

(Received xx; revised xx; accepted xx)

In this study, we investigate the characteristics of three-dimensional turbulent boundary layers influenced by transverse flow and pressure gradients. Our findings reveal that even without assuming an infinite sweep, a fully developed turbulent boundary layer over the present swept blunt body maintains spanwise homogeneity, consistent with infinite sweep assumptions. We critically examine the law-of-the and temperature-velocity relationships, typically applied two-dimensional turbulent boundary layers, in three-dimensional contexts. Results show that with transverse velocity and pressure gradient, streamwise velocity adheres to classical velocity transformation relationships and the predictive accuracy of classical temperature-velocity relationships diminishes because of pressure gradient. We show that near-wall streak structures persist and correspond with energetic structures in the outer region, though three-dimensional effects redistribute energy to align more with the external flow direction. Analysis of shear Reynolds stress and mean flow shear directions reveals in near-wall regions with low transverse flow velocity, but significant deviations at higher transverse velocities. Introduction of transverse pressure gradients together with the transverse velocities alter the velocity profile and mean flow shear directions, with shear Reynolds stress experiencing similar changes but with a lag increasing with transverse. Consistent directional alignment in outer regions suggests a partitioned relationship between shear Reynolds stress and mean flow shear: nonlinear in the inner region and approximately linear in the outer region.

Key words:

MSC Codes (*Optional*) Please enter your MSC Codes here

1. Introduction

Boundary layer flows in practical engineering problems are generally turbulent and three-dimensional. However, to date, most theoretical, experimental, and numerical simulation

† Email address for correspondence: xiyc@mail.tsinghua.edu.cn

studies on turbulent boundary layers have been confined to two-dimensional boundary layers. These studies have provided fundamental characteristics of turbulent boundary layers and have guided the development of turbulence models, such as Reynolds-Averaged Navier-Stokes (RANS) models.

Although there have been some studies on three-dimensional turbulent boundary layers, such as the experimental study of a three-dimensional supersonic turbulent boundary layer induced by a curved fin (Konrad & Smits 1998), the three-dimensional shock-wave/turbulent boundary-layer interactions (Gaitonde & Adler 2023), the three-dimensional turbulent boundary layer over a model lifting body (Dong *et al.* 2024), these investigations are mostly case-specific, and the relationships between three-dimensional and two-dimensional turbulent boundary layers remain unclear. Recently, we conducted simulations of the attachment-line boundary layer of a hypersonic leading edge. We realized that this configuration serves as a natural model to bridge two-dimensional and three-dimensional turbulent boundary layers: In the attachment-line region, the flow approximates a two-dimensional turbulent boundary layer, whereas as the flow develops downstream along the chordwise direction, away from the attachment-line region, its three-dimensional characteristics gradually become more pronounced. This progression evolves the flow from a two-dimensional to a three-dimensional turbulent boundary layer. Therefore, the swept blunt body model can be considered a standardized model for studying three-dimensional turbulent boundary layers.

This paper is the second part of our study on the numerical simulations of attachment-line boundary layer in hypersonic flow. In the first part, the roughness-induced subcritical transitions of attachment-line boundary layer for a swept blunt body have been studied. Two roughness elements of different heights are examined. For the lower-height roughness element, additional unsteady perturbations are required to trigger a transition in the wake, suggesting that the flow field behind the roughness element acts as a disturbance amplifier for upstream perturbations. Conversely, a higher roughness element can independently induce the transition. A low-frequency absolute instability is detected behind the roughness, leading to the formation of streaks. The secondary instabilities of these streaks are identified as the direct cause of the final transition. Following the transition of the boundary layer to a fully developed turbulent state, we continued our computations further downstream. The analysis of this fully developed turbulent boundary layer in the downstream region is the core of this study.

In this paper, we describe the general characteristics of three-dimensional turbulent boundary layers in this configuration, focusing on the properties of the mean flow and low-order turbulence statistics. This paper is organized as follows. The methodology and models of this study are also presented for the sake of completeness of the paper in section 2. The major results of the three-dimensional turbulent boundary are shown in section 3 and the conclusions are given in section 4.

2. Methodology

The governing equations for all simulations in this work are the dimensionless compressible Navier–Stokes (NS) equations for a Newtonian fluid, which can be written as:

$$\frac{\partial Q}{\partial t} + \frac{\partial F_j}{\partial x_j} + \frac{\partial F_j^v}{\partial x_j} = 0, \quad (2.1)$$

$$Q = [\rho, \rho u_1, \rho u_2, \rho u_3, E_t]^T, \quad (2.2)$$

$$F_j = \begin{bmatrix} \rho u_j \\ \rho u_1 u_j + p \delta_{1j} \\ \rho u_2 u_j + p \delta_{2j} \\ \rho u_3 u_j + p \delta_{3j} \\ (E_t + p) u_j \end{bmatrix}, F_j^v = \begin{bmatrix} 0 \\ \tau_{1j} \\ \tau_{2j} \\ \tau_{3j} \\ \tau_{jk} u_k - q_j \end{bmatrix}. \quad (2.3)$$

Throughout this work the coordinates x_i , ($i = 1, 2, 3$) are referred to as x, y, z , respectively, with corresponding velocity components $u_1 = u, u_2 = v, u_3 = w$. F_j and F_j^v stand for the inviscid and viscous flux. The total energy E_t and the viscous stress τ_{ij} are given as, respectively,

$$E_t = \rho \left(\frac{T}{\gamma(\gamma - 1)M_\infty^2} + \frac{u_k u_k}{2} \right), \quad (2.4)$$

$$\tau_{ij} = \frac{\mu}{Re_\infty} \left(\frac{\partial u_i}{\partial x_j} + \frac{\partial u_j}{\partial x_i} - \frac{2}{3} \delta_{ij} \frac{\partial u_k}{\partial x_k} \right).$$

The pressure p and heat flux q_i are obtained from:

$$p = \frac{\rho T}{\gamma M_\infty^2}, \quad q_i = -\frac{\mu}{(\gamma - 1)M_\infty^2 Re_\infty Pr} \frac{\partial T}{\partial x_i}. \quad (2.5)$$

The viscosity is calculated using the Sutherland law

$$\mu = T^{3/2} \frac{T_\infty + C}{T \cdot T_\infty + C}, \quad (2.6)$$

with $C = 110.4K$. The free-stream Reynolds number Re_∞ , Mach number M_∞ and Prandtl number Pr are defined as

$$Re_\infty = \frac{\rho_\infty^* U_\infty^* l_0^*}{\mu_\infty^*}, \quad M_\infty = \frac{U_\infty^*}{\sqrt{\gamma R_g^* T_\infty^*}}, \quad Pr = 0.72, \quad (2.7)$$

where ρ_∞^* , U_∞^* , T_∞^* and μ_∞^* stand for the freestream density, velocity, temperature and viscosity, respectively. $R_g^* = 287J/(K \cdot Kg)$ represents the specific gas constant and $\gamma = 1.4$ stands for the ratio of specific heat. The length scale l_0^* is chosen as 1 millimeter in this research. The * denotes dimensional flow parameters in this section.

The computational model is designed based on the recent experimental test and the schematics of the model are shown in figure 1. The computational model can be likened to a sandwich-like configuration, where the top and bottom layers consist of semicircles with a radius of $R_1 = 17.5mm$, and the intermediate layer is a flat plate with a width of 5mm. Together, these three layers form the complete swept blunt body configuration. The roughness elements is located at $z = L_2 = 40mm$, at the center of the leading plate. The radius of the roughness is $R_2 = 2mm$. The length of the whole model is designed as $L_1 = 200mm$. Based on experiments, the surface temperature is set to $T_w^* = 370K$. The blunt leading edge is placed in a hypersonic flow of $M_\infty = 6.0$, the swept angle is $\Lambda = 45^\circ$ and the temperature of the incoming flow is set to 56.58K according to experimental conditions. Grids that used in the present simulations are presented in table 1, based on wall units. Based on that grid size, as there are no additional stress and heat flux terms in the present simulations, resolutions for an implicit large-eddy simulations (ILES) can be recognized for the turbulent region. More details about the numerical methods, the strategies, the computational grids and boundary conditions used for performing simulations have already been presented in the first part of this series of study. The H0200 cases in the first part of this series of study is used for further analysis.

It is important to note that our calculations are based on results obtained from ILES, rather

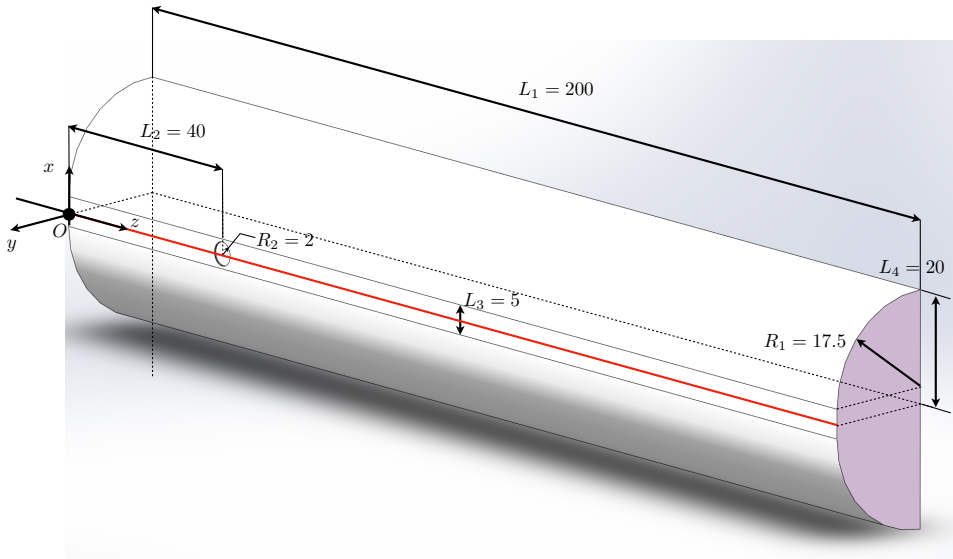
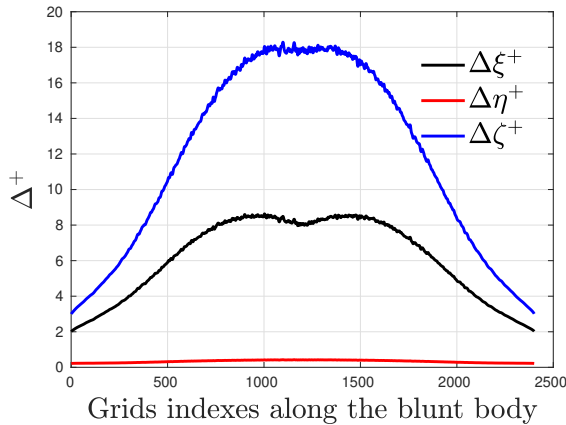


Figure 1: Schematics of the swept blunt leading edge used for numerical simulations.

than DNS, some specific quantitative trends or small scale features may exhibit deviations. However, the first-order statistical quantities and mean-flow results are considered to be reliable. Based on our experience, the grid requirements for DNS of general supersonic three-dimensional boundary layers are as follows: The grid spacing in the two directions parallel to the wall, based on wall units, should ideally be isotropic and satisfy the criteria $\Delta\xi \approx \Delta\zeta \leq 4$; The grid spacing in the wall-normal direction should meet the specified requirement $\Delta\eta \leq 0.5$. These lead to the condition that effective mesh spacing $\Delta \approx (\Delta\xi \times \Delta\zeta \times \Delta\eta)^{1/3}$ is always smaller than two times the local Kolmogorov length scale. Also, there should be at least 100–200 points within the boundary layer. These conditions ensure the grid convergence of high-order turbulence statistics (with errors less than 0.1%). Given the conditions of the present configuration, we need approximately 8 times more grids than we currently have to resolve all the scales, which exceeds our existing computational capabilities.

To analyze the characteristics of the turbulent boundary layer flow, we extracted a fully developed turbulent section of the previously computed three-dimensional transitional boundary layer along the spanwise direction for detailed analysis. To facilitate the analysis investigating the mean field characteristics, both Reynolds-averaged and Favre-averaged mean quantities are employed, following the approach of [Huang *et al.* \(1995\)](#). The Reynolds-averaged mean of an arbitrary variable f is denoted by \bar{f} , while the Favre-averaged mean is denoted by $\tilde{f} = \overline{\rho f} / \bar{\rho}$. In addition, the fluctuations around the Reynolds and Favre averages are represented by single and double primes, respectively. That is, $f' = f - \bar{f}$ and $f'' = f - \tilde{f}$. Given the absence of homogeneous directions in the configurations under consideration, achieving ideally averaged states necessitates a considerable amount of time. The statistical analysis of the flows was conducted over a span of 1800 time units, encompassing approximately 900,000 steps. This duration is roughly sixfold the time required for a flow to evolve from the inlet to the spanwise flow outlet. To ascertain the independence of flow statistics from the duration of statistical analysis, we performed an additional test. This test involved comparing flow statistics derived from two distinct averaging intervals, with one interval containing 50% more statistical steps than the other, to ensure that any



ξ	η	ζ	Total points	$\Delta\xi_{max}^+$	$\Delta\eta_{max}^+$	$\Delta\zeta_{max}^+$
2401	601	4401	6.35×10^9	8.5	0.4	18.2

Table 1: Grid points and maximum grid sizes in wall units at the turbulent boundary region.

discrepancies of the flow statistics for major variables between the two intervals were small enough, not exceeding 0.1%.

Some common variables are defined along the whole three-dimensional surface. Here, as the usual boundary layers in previously, we define the velocity \bar{u}^+ , based on inner scale as

$$\left. \begin{aligned} \bar{u}^+ &= \frac{|\bar{u}_p|}{\bar{u}_\tau}, & |\bar{u}_p| &= \sqrt{\bar{u}_\xi^2 + \bar{w}^2}, & h^+ &= \frac{\bar{\rho}_w \bar{u}_\tau h}{\bar{\mu}_w}, \\ \bar{u}_\tau &= \sqrt{\frac{\bar{\tau}_w}{\bar{\rho}_w}}, & \bar{\tau}_w &= \frac{\bar{\mu}}{Re} \frac{\partial \bar{u}_p}{\partial h} \Big|_{h=0}, & h^* &= \frac{\bar{\rho} \sqrt{\bar{\tau}_w} / \rho h}{\bar{\mu}} \end{aligned} \right\}, \quad (2.8)$$

where, \bar{u}_p is the velocity parallel to the surface and \bar{u}_ξ is also the velocity parallel to the surface but confined to the $x - y$ plane. The skin-friction coefficient C_f and surface heat-flux θ_{tw} for this kind of flow are defined as

$$C_f = \frac{2\bar{\mu}_w^*}{\rho_\infty^* U_\infty^{*2}} = \frac{2\bar{\mu}_w}{Re} \frac{\partial \bar{u}_p}{\partial h} = 2\bar{\tau}_w, \theta_{tw} = - \left| \kappa \nabla T \cdot \mathbf{n} \right|. \quad (2.9)$$

The derivatives of surface normals, denoted as $\partial/\partial h$, for arbitrary variables f_ψ , are determined through a two-step process. Initially, the gradients of the variables f_ψ are computed utilizing the identical scheme adopted for the calculation of viscous fluxes during the simulations. Subsequently, the derivatives of the surface normals $\partial f_\psi / \partial h$ are obtained by projecting the calculated gradients ∇f_ψ onto the surface normal vectors \mathbf{n} . The thickness of boundary layer δ_{99} is mainly defined based on spanwise velocity as the wall-normal distance from the wall to the location where $\bar{w} = 0.99\bar{w}_e$.

3. Results

3.1. Validation of the numerical results

Before conducting the related analysis, it is crucial to first verify the reliability of the data obtained from the current simulation. This is particularly challenging in compressible flows. Unlike incompressible flows, compressible flows lack sufficient experimental data support, mainly because accurate measurements in the supersonic regime are very difficult (Smits & Dussauge 2005; Gatski & Bonnet 2013). For general high Mach number three-dimensional compressible boundary layers, this is undoubtedly even more challenging. Fortunately, in our current designed case, we can somewhat refer back to two-dimensional boundary layers, at least along the attachment line, where the flow reverts to a statistically two-dimensional boundary layer. Consequently, validation of the present data is conducted by comparing the characteristics of the boundary layer along the attachment line. For compressible two-dimensional boundary layers, Morkovin's hypothesis (Morkovin 1962) is generally considered valid, which posits that compressibility effects do not alter the time and length scales of turbulence. By considering the density variations in the turbulent boundary layer region, compressible turbulence can be analogized to incompressible turbulence through local parameters. Then, the scaled Reynolds stress can be written as

$$\left. \begin{aligned} (u_i^*)^2 &= \frac{\bar{\rho}}{\bar{\rho}_w} \frac{\widetilde{u_i''^2}}{\bar{u}_\tau^2}, & i = 1, 2, 3 \\ (u_i u_j)^* &= \frac{\bar{\rho}}{\bar{\rho}_w} \frac{\widetilde{u_i'' u_j''}}{\bar{u}_\tau^2}, & i \neq j \end{aligned} \right\}, \quad (3.1)$$

which should collapse the data to the incompressible ones. Here, \bar{u}_τ is the friction velocity and subscript w represents the variables at the wall surface. The results of an incompressible turbulent boundary layer at $Re_\tau = 445$ simulated by Jiménez *et al.* (2010) and a compressible turbulent boundary layer at $Re_\tau = 453$ simulated by Cogo *et al.* (2022) are used as references. The comparison for major components of Reynolds stress is shown in figure 2. All calculated profiles are presented as a function of the semilocal scaling h^* , which is based on τ_w and local properties, proposed by Huang *et al.* (1995). In the figure, the black solid line represents the spanwise-transformed Reynolds stress component $(w^*)^2$. The red and blue solid lines indicate the Reynolds stress components in the x -direction $(u^*)^2$ and the wall-normal y -direction $(v^*)^2$, respectively. The black dashed line represents the shear Reynolds stress component $(wv)^*$. As can be viewed, the computed and statistically analyzed Reynolds stresses at the exact attachment line generally align with the results obtained from direct numerical simulations for both incompressible and compressible flat-plate boundary layers. The peak values and shapes of the Reynolds stresses in the streamwise direction are consistent with the corresponding reference values. This agreement validates the resolution of our current computational setup. However, the Reynolds stresses in the wall-normal and chordwise directions are smaller than the reference values. This discrepancy is likely due to the influence of the leading-edge shock wave and the chordwise pressure gradient in the conditions of this study. At the leading edge, the height of the shock wave from the wall is approximately 13mm, which is about sixteen times the turbulent boundary layer thickness at that location. This suppresses the development of fluctuations in this direction, resulting in lower corresponding Reynolds stresses $(v^*)^2$. Along the chordwise direction at the leading edge, the condition $\partial/\partial x = 0$ is satisfied only at the exact attachment line ($x = 0$), hence the Reynolds stresses $(u^*)^2$ in this direction are also somewhat suppressed.

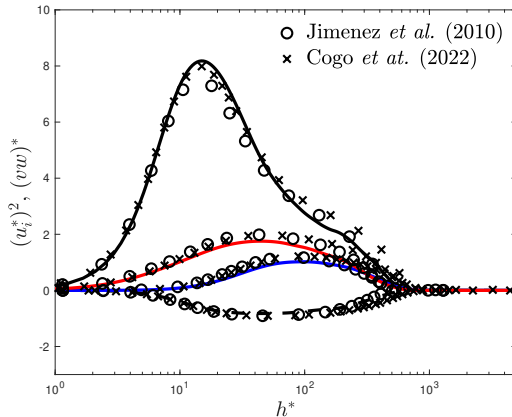


Figure 2: Comparison of the scaled Reynolds stress obtained from the current simulation with the reference values at the spanwise location $z = 145.5$.

3.2. General features of the turbulent boundary layer

3.2.1. Mean field

The laminar and transitional boundary layer have been documented in the previous study. Here, we focus on the turbulent section. The basic features of turbulent boundary layer are reflected in their profiles along the wall normal directions. The profiles for major variables along the wall normal direction, at several locations, are shown in figure 3 and 4. It can be observed that as the attachment-line boundary layer develops from the upstream position ($z = 136.3$) to the downstream position ($z = 163.6$), the boundary layer does not thicken as expected for a well-known flat plate boundary layer. Instead, the thickness of the boundary layer remains almost constant. This indicates that the fully developed turbulent attachment-line boundary layer can also reach a corresponding asymptotic state, in the present cases. By broadening our perspective further, it becomes evident that this assumption remains valid even in regions where crossflow effects are significant, as demonstrated in figure 4. All these phenomena indicate that, under the conditions of our study, the development of the turbulent boundary layer in the wall-normal η -direction as well as the spanwise z -direction are inhibited, and the boundary layer does not thicken in the spanwise direction.

Away from the attachment-line, unlike traditional two-dimensional boundary layers, the presence of pressure gradients in three-dimensional boundary layers induces a crossflow component. The three-dimensional boundary layer are most conveniently described in a local streamline coordinate system as shown in figure 5(a), the main streamwise and the crossflow directions are defined based on the angle of external streamlines $\theta_s = \arctan(\bar{u}_{\xi,e}/\bar{w}_e)$ at the edge of the turbulent boundary layer. The streamwise and the crossflow velocities are defined as

$$\left. \begin{aligned} u_s &= \bar{w} \cos \theta_s + \bar{u}_{\xi} \sin \theta_s, \\ u_c &= -\bar{w} \sin \theta_s + \bar{u}_{\xi} \cos \theta_s. \end{aligned} \right\} \quad (3.2)$$

As shown in figure 5(b), when the wall surface is approached, the magnitude of the crossflow velocity u_c (the red lines) increases from small value at the edge of boundary layer, reaches a maximum value, and then decreases back to zero at the wall surface to satisfy the no-slip condition. In contrast, the behaviour of the streamwise velocity u_s (the blue lines) is qualitatively similar to that in two-dimensional boundary layers. The direction of the wall shear stress vector $\bar{\tau}_w$ determines the tangent to the limiting streamline at the wall. In general, the angle between the tangents to the external streamline and the limiting streamline at the

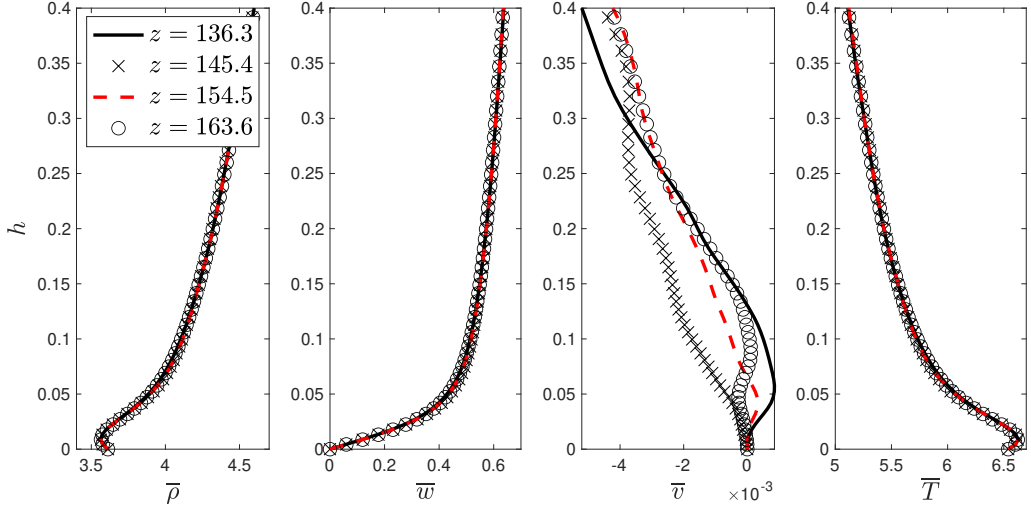


Figure 3: The wall-normal profiles of mean-flow variables at the attachment-line plane.

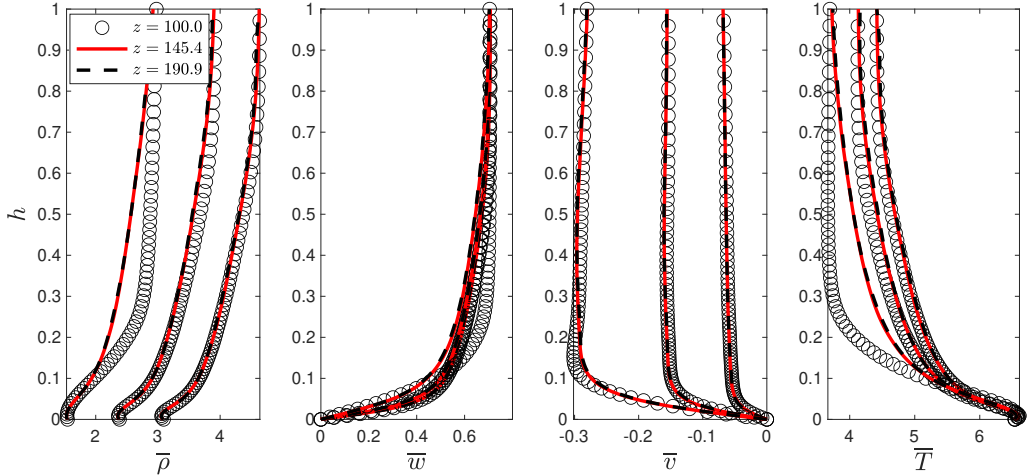


Figure 4: The distributions for mean-flow variables with wall normal direction at the chordwise location $s_{\xi} = 8.71$, $s_{\xi} = 13.50$ and $s_{\xi} = 18.61$.

wall surface is non-zero. As a result, when acrossing the hight of the boundary layer, the velocity vector rotates through an angle at the wall (the transparent grey lines). Similarly, the shear stress vector tends to rotate away from its direction at the wall as the distance from the surface increases.

As shown in figure 6, when the flow develops from the attachment line to chordwise downstream, the pressure gradient increases (figure 6(a)), leading to stronger crossflow velocities (figure 6(b – e)). Consequently, the boundary layer becomes thicker, and the rotation of the velocity vectors within the boundary layer becomes more pronounced.

3.2.2. fluctuation field

Then, we establish an intuitive visualization of the three-dimensional turbulent boundary layer flow by presenting the distribution of instantaneous or fluctuated variables contours at different sections. The instantaneous density contours in several selected cross sections are

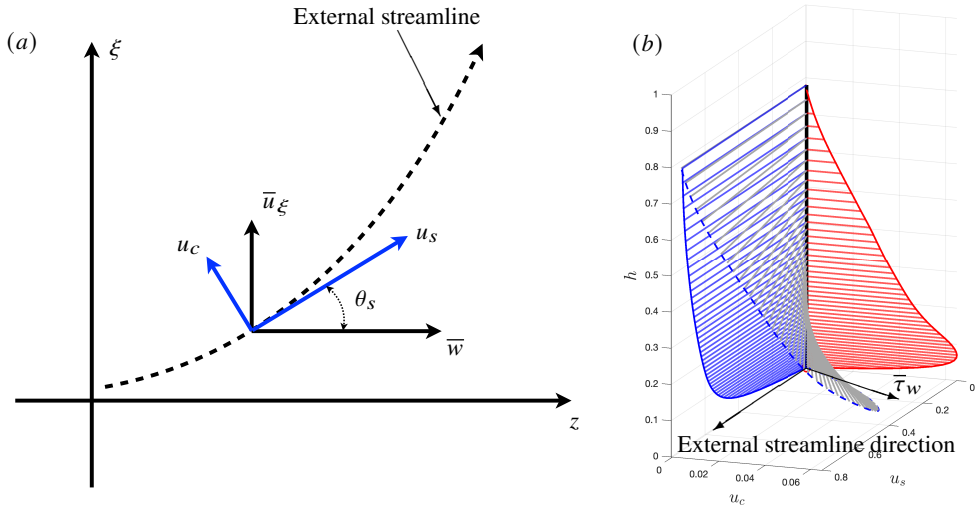


Figure 5: (a) Schematic of a local streamline coordinate system and (b) Three dimensional velocity profiles of the present simulations at chordwise location $s_\xi = 13.50$.

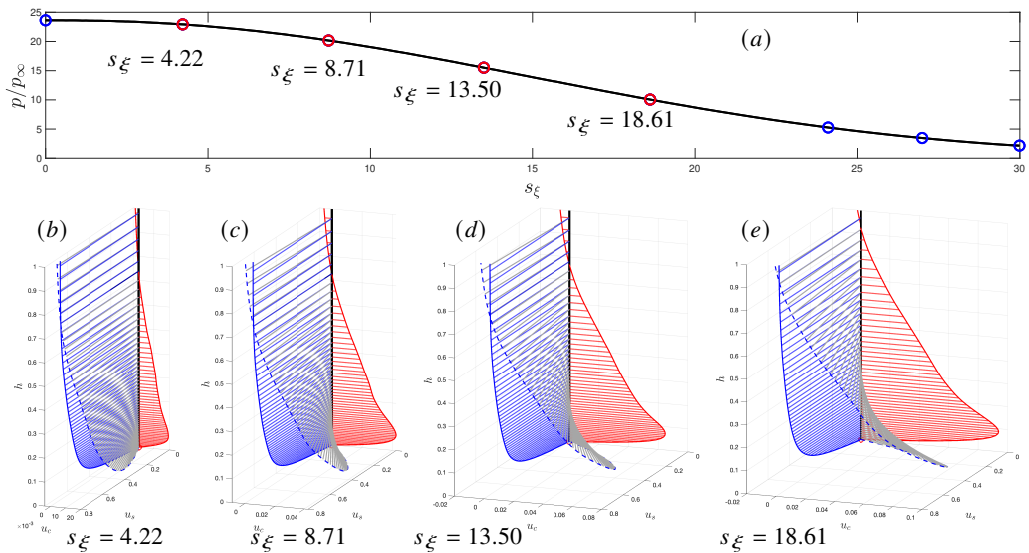


Figure 6: (a) The pressure distributions along the surface. (b – e) Three dimensional velocity profiles of the present simulations at several chordwise location, ranging from the attachment-line region to chordwise downstream. The specific locations corresponding to the three-dimensional velocity profiles are sequentially marked with red circles in (a).

shown in figure 7(c), ranging from attachment line to chordwise exit. The exact locations of these slices are shown in figure 7(a) and (b). The contour exhibits the typical structure, already found in flat-plate turbulent boundary layers (Smith & Smits 1995; Pirozzoli & Bernardini 2011; Duan *et al.* 2014; Cogo *et al.* 2022), dominated by large-scale patterns inclined at some angle. Therefore, simply observing the characteristics on a single cross-section makes it difficult to distinguish between two-dimensional and three-dimensional boundary layers. As a supplement, some nearly wall-parallel slices for instantaneous density contours are shown in figure 8. From the attachment line to the chordwise exit, the density

perturbations become sparser as the density amplitude decreases (changing from red to blue). With increasing distance from the wall (from Figure 8(a) to Figure 8(c)), the characteristic structures of the perturbations grow larger. Near the wall, the disturbance structures exhibit a clear preferential orientation, and it can be faintly observed that the disturbance structures gradually shift from the spanwise direction to the chordwise direction.

To obtain clearer images of the disturbances themselves, we subtract the mean flow to observe the fluctuations. Figures 9 and 10 show contours of the instantaneous spanwise velocity fluctuations w' and temperature fluctuations T' for the present cases in nearly wall-parallel slices taken at three different locations, standing for both the inner ($h^+ = 15.5$) and outer region ($h/\delta_{99} = 0.18/0.53$) at the selected stations.

As seen in figure 9(a), the spanwise velocity field in the inner layer presents the typical streaky pattern. These streaky patterns are distributed along the spanwise z -direction in the attachment line region. As the chordwise distance s_ξ increases, these structures tend to align with the direction of the external streamline. Therefore, all these patterns exhibit a certain radiating state, appearing as skirt-like structures extending from the attachment line along the chordwise direction. Similar visualizations of near-wall streaks in flat-plate boundary layer simulations were also reported by (Duan *et al.* 2010; Pirozzoli & Bernardini 2011; Duan *et al.* 2011; Cogo *et al.* 2022). These findings suggest that the near-wall streak structures in the three-dimensional turbulent boundary layer resemble those in a two-dimensional flat-plate turbulent boundary layer, both aligning with the direction of the external streamline. The alternating distribution of high and low momentum zones forms the velocity streak structures depicted in this figure. This formation is associated with ejection and sweep events. These large-scale structures can extend several boundary layer thicknesses in the direction of the external streamline and contain a significant portion of the turbulent kinetic energy. As the slice move away from the surface (figure 9(b)), a qualitatively similar pattern found in figure 9(a) are also presented on a much larger scale. These structures can be identified as outer-layer streaks, which can be identified as large scale coherent structures or "superstructures" in outer region (Ganapathisubramani *et al.* 2006; Hutchins & Marusic 2007). From this perspective, the near-wall small-scale structures appear to be the footprints of the large-scale structures from the outer layer in the near-wall region. This observation is also consistent with what has been previously understood in flat-plate boundary layers. The scenario changes significantly as the nearly surface-parallel plane moves further away, the flow becomes extremely intermittent, as present in figure 9(c).

The temperature field in the same layers (Figure 10(a – c)) also reveals a similar picture. The figures (a) and (b) exhibit clear streak structure, which is qualitatively similar to that of spanwise velocity fluctuations w' . Upon closer inspection, one can observe a close correspondence between zones with positive temperature fluctuations (red regions) and low-speed streaks (blue regions), and vice versa. This is a typical manifestation of the well-known tendency for velocity and temperature fluctuations in shear flows to be negatively correlated. In this case, it is a consequence of the fact that outward wall-normal motions transport negative velocity fluctuations and positive temperature fluctuations from the inner, low-speed, high-temperature layers to the upper layers. Similar observations have been elucidated in previous studies in flat-plate boundary layer by Pirozzoli & Bernardini (2011).

All these observations tell us that the typical near-wall disturbance structures in two-dimensional and three-dimensional turbulent boundary layers are very similar. However, due to the modulation effect of the mean flow, these flow structures exhibit a strong tendency to align with the direction of the external flow.

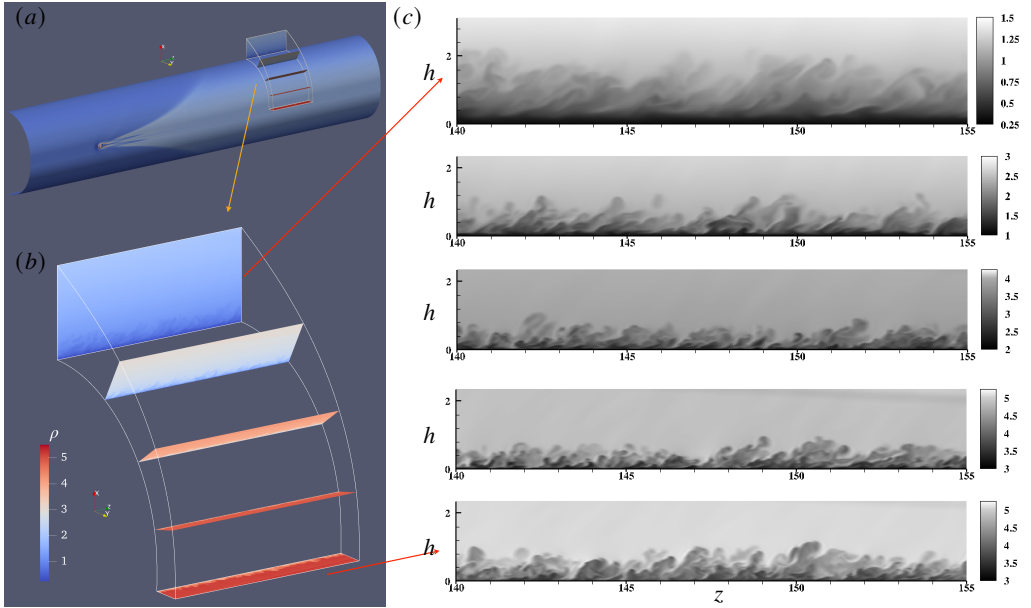


Figure 7: (a) Schematics of the swept blunt leading edge with the average surface skin friction $\bar{\tau}_w$ and the selected region. (b) the enlarged figure for the region selected in (a). (c) the instantaneous density of the selected cross-sections in (a) and (b).

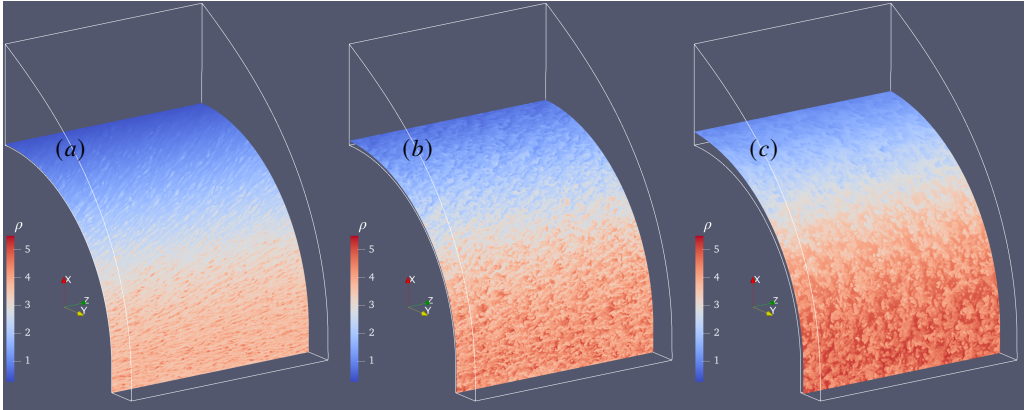


Figure 8: (a – c) stand for instantaneous density ρ distributions at spanwise cross sections at grid index $\eta = 33$ ($h^+ = 15.5$), 101 ($h/\delta_{99} = 0.18$) and 201 ($h/\delta_{99} = 0.53$), respectively. h^+ , h and δ_{99} are defined based on the variables at exact attachment-line plane. $\delta_{99} \approx 0.8$ at the present case.

3.3. Law-of-the-wall and velocity-temperature relationships

3.3.1. Law-of-the-wall

All prior researches on mean velocity transformations in compressible turbulent boundary layers was mainly confined to statistically two-dimensional boundary layers, hence their performance in actual three-dimensional boundary layers remains largely unknown. Here, we will conduct a study of velocity transformations, in an attempt to further elucidate the impact of three-dimensional effects and pressure gradients on the effectiveness of these compressibility transformations.

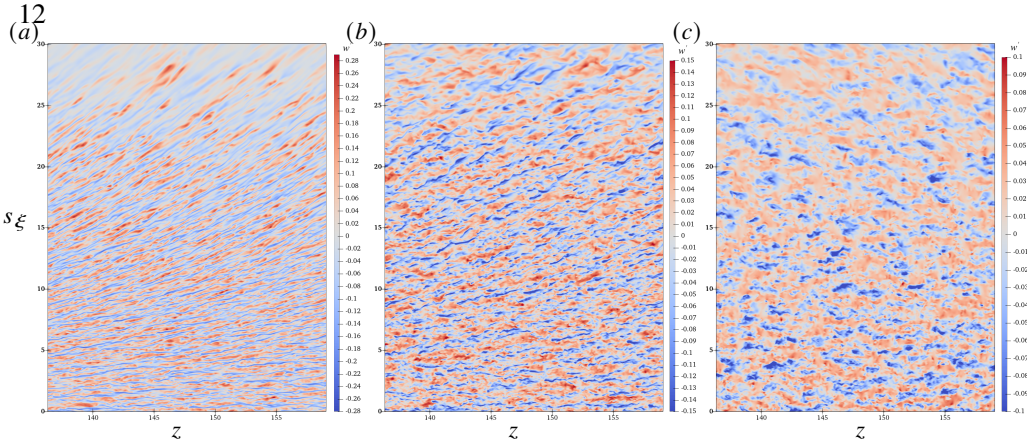


Figure 9: (a – c) stand for spanwise fluctuations w' at the cross sections at grid index $\eta = 33, 101$ and 201 , respectively.

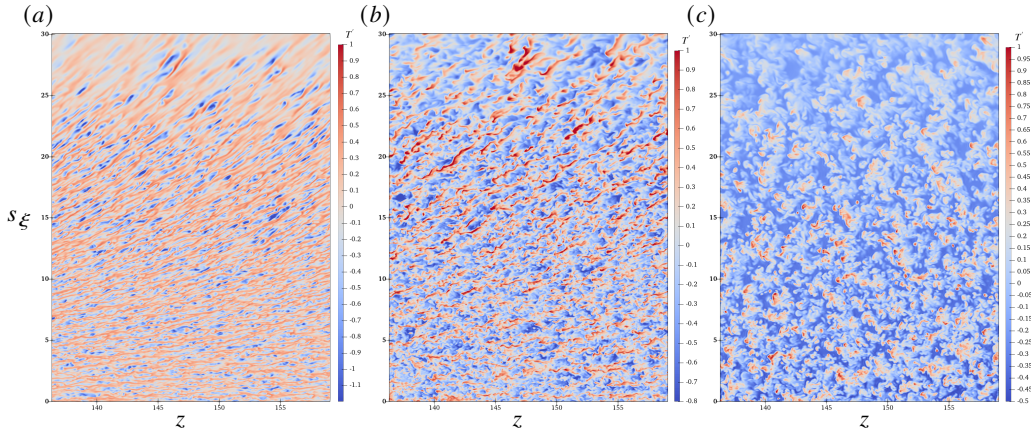


Figure 10: (a – c) stand for temperature fluctuations T' at the cross sections at grid index $\eta = 33, 101$ and 201 , respectively.

As analyzed in the previous mean flow analysis, in a typical three-dimensional boundary layer, the velocity vector parallel to the wall can point in any direction, and this direction changes with the height away from the wall. Therefore, directly transforming the mean velocity parallel to the wall, as done in a two-dimensional flat-plate boundary layer, is not meaningful, since the direction of the velocity vector is not uniform. Thus, we need to decompose this velocity vector into two different directions to ensure the uniformity of the velocity vector direction. One can simply decompose and project the velocity vector onto the spanwise z -direction and the chordwise ξ -direction. The reason to chose these two directions is that, in the current three-dimensional boundary layer, the pressure gradient exists only in the $x - y$ plane and not in the spanwise z -direction. By using this decomposition, one can decouple the pressure gradient effects from the flow in a specific direction. Therefore, in each chordwise location, except the exact attachment line, two velocities w and u_ξ along the z and ξ directions, are used to assess various compressibility scaling relations in case of three dimensional flows. However, from a statistical perspective, in regions very close to the attachment line, the values of u_ξ are very small over a substantial area, thus showing limited significance. Instead, we chose the mainstream velocity direction u_s parallel to the external streamline as the second velocity vector to characterize the three-dimensional flow

The van Driest transformation(Van Driest 1951) is widely used to transform the mean

velocity profile in a compressible boundary layer to a profile from an incompressible boundary layer by taking the variations of mean density into account. In general three-dimensional boundary layer, the velocity vector parallel to the wall surface can be In the present three dimensional boundary layer, the similar form in the present study can be taken as:

$$w_{VD}^+ = \int_0^{\bar{w}^+} \sqrt{\frac{\bar{\rho}}{\bar{\rho}_w}} d\bar{w}^+, \quad u_{sVD}^+ = \int_0^{\bar{u}_s^+} \sqrt{\frac{\bar{\rho}}{\bar{\rho}_w}} d\bar{u}_s^+ \quad (3.3)$$

This transformation works well in collapse velocity profiles in normal adiabatic boundary layer flows. However, in diabatic boundary layers, the transformation fails and can not collapse into the incompressible law of the wall. [Trettel & Larsson \(2016\)](#) proposed a new transformation based on the stress-balance conditions and can be written as

$$\left. \begin{aligned} w_{TL}^+ &= \int_0^{\bar{w}^+} \sqrt{\frac{\bar{\rho}}{\bar{\rho}_w}} \left[1 + \frac{1}{2\bar{\rho}} \frac{\partial \bar{\rho}}{\partial h} h - \frac{1}{\bar{\mu}} \frac{\partial \bar{\mu}}{\partial h} h \right] d\bar{w}^+, \\ u_{sTL}^+ &= \int_0^{\bar{u}_s^+} \sqrt{\frac{\bar{\rho}}{\bar{\rho}_w}} \left[1 + \frac{1}{2\bar{\rho}} \frac{\partial \bar{\rho}}{\partial h} h - \frac{1}{\bar{\mu}} \frac{\partial \bar{\mu}}{\partial h} h \right] d\bar{u}_s^+, \\ h^* &= \frac{\bar{\rho}}{\bar{\mu}} \sqrt{\frac{\bar{\tau}_w}{\bar{\rho}}} h \end{aligned} \right\} \quad (3.4)$$

The Trettel & Larsson transformation is functioning well in collapsing the profiles for a non-adiabatic turbulent boundary layer to an equivalent incompressible profile, especially for channel flow. Their performances in boundary layers are not that good. To improve the overall collapse of the mean velocity profile in boundary layers, [Volpiani *et al.* \(2020\)](#) developed a new transformation based on data-driven approaches, this transformation can be written as

$$w_V^+ = \int_0^{\bar{w}^+} \sqrt{\frac{\bar{\rho}/\bar{\rho}_w}{\bar{\mu}/\bar{\mu}_w}} d\bar{w}^+, \quad u_{sV}^+ = \int_0^{\bar{u}_s^+} \sqrt{\frac{\bar{\rho}/\bar{\rho}_w}{\bar{\mu}/\bar{\mu}_w}} d\bar{u}_s^+, \quad h_V^+ = \int_0^{\bar{h}^+} \sqrt{\frac{\bar{\rho}/\bar{\rho}_w}{(\bar{\mu}/\bar{\mu}_w)^3}} dh^+ \quad (3.5)$$

[Griffin *et al.* \(2021\)](#) further introduced a new transformation, which involves scaling the viscous stress through semi-local non-dimensionalization within the viscous sublayer, and addressing the Reynolds shear stress to preserve the approximate balance between turbulence production and dissipation in the log-law region. This transformation has been demonstrated to effectively unify the velocity profiles across a diverse array of flows, encompassing heated, cooled, and adiabatic boundary layers, as well as fully developed channel and pipe flows. The transformation is referred to the total-stress-based transformation, can be written as

$$\left. \begin{aligned} w_{TS}^+ &= \int_0^{\bar{w}^+} \frac{S_{eq,w}^+}{1 + S_{eq,w}^+ - S_{TL,w}^+} dh^*, \quad S_{eq,w}^+ = \frac{\bar{\mu}_w}{\bar{\mu}} \frac{\partial w^+}{\partial h^*}, \quad S_{TL,w}^+ = \frac{\bar{\mu}}{\bar{\mu}_w} \frac{\partial w^+}{\partial h^*}, \\ u_{s,TS}^+ &= \int_0^{\bar{u}_s^+} \frac{S_{eq,u_s}^+}{1 + S_{eq,u_s}^+ - S_{TL,u_s}^+} dh^*, \quad S_{eq,u_s}^+ = \frac{\bar{\mu}_w}{\bar{\mu}} \frac{\partial u_s^+}{\partial h^*}, \quad S_{TL,u_s}^+ = \frac{\bar{\mu}}{\bar{\mu}_w} \frac{\partial u_s^+}{\partial h^*}, \end{aligned} \right\} \quad (3.6)$$

The transformed spanwise and streamwise velocity profiles at several chordwise locations are shown in figures 11 and 12, ranging from the exact attachment line to downstream chordwise direction. Firstly, we look at the profiles at the exact attachment line (Figure 11(a) and Figure 12(a)). Excluding the Trettel & Larsson transformation, the other three transformations yielded satisfactory results. Based on previous research, the Trettel & Larsson transformation is expected to perform well in fully developed, non-spatially varying boundary

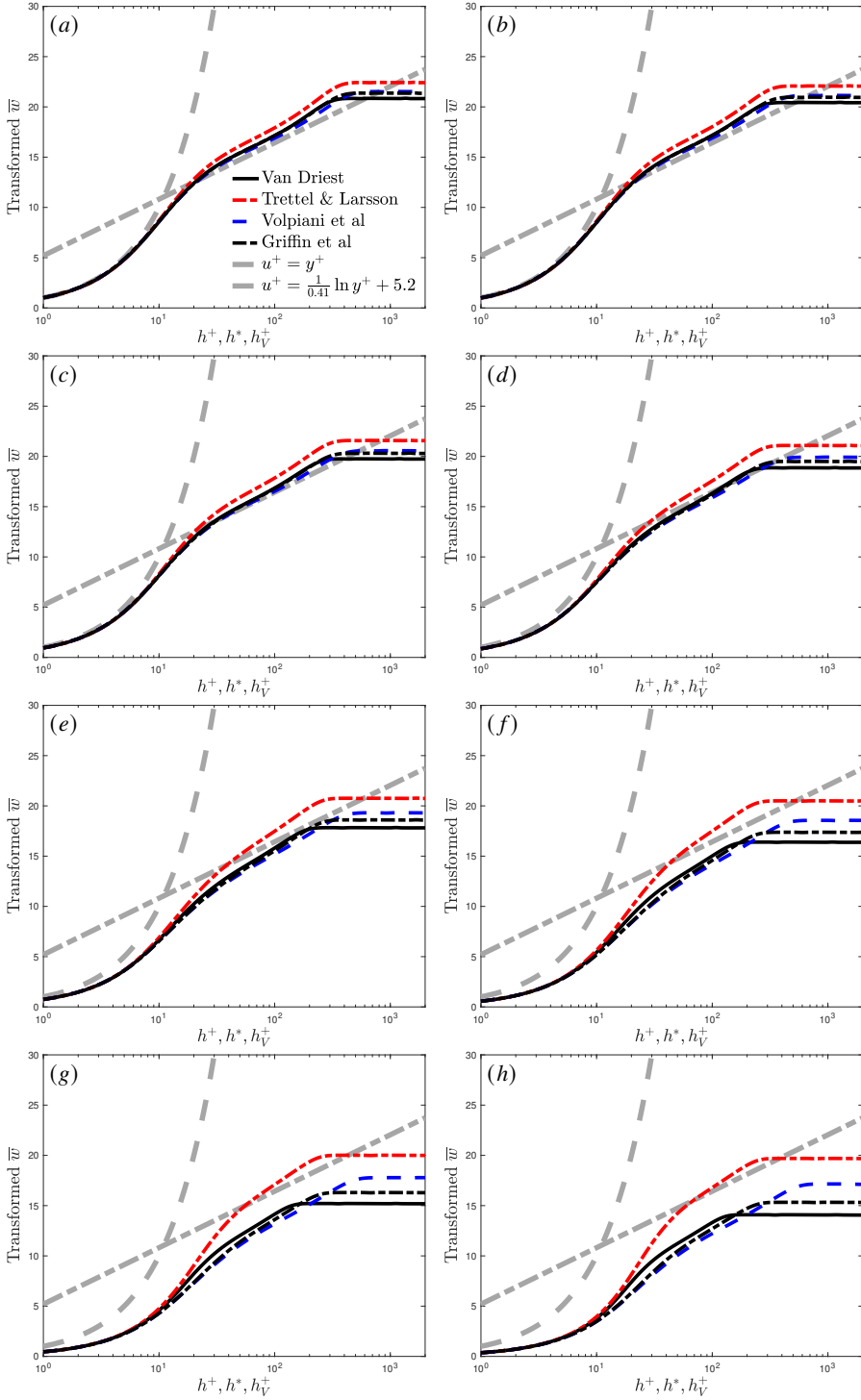


Figure 11: Spanwise mean-velocity profiles, transformed according to several transformations, at different chordwise locations. (a) – (h) stand for the location at chordwise $s_{\mathcal{E}} = 0.00, 4.22, 8.71, 13.50, 18.61, 24.10, 26.99$ and 30.00 , respectively.

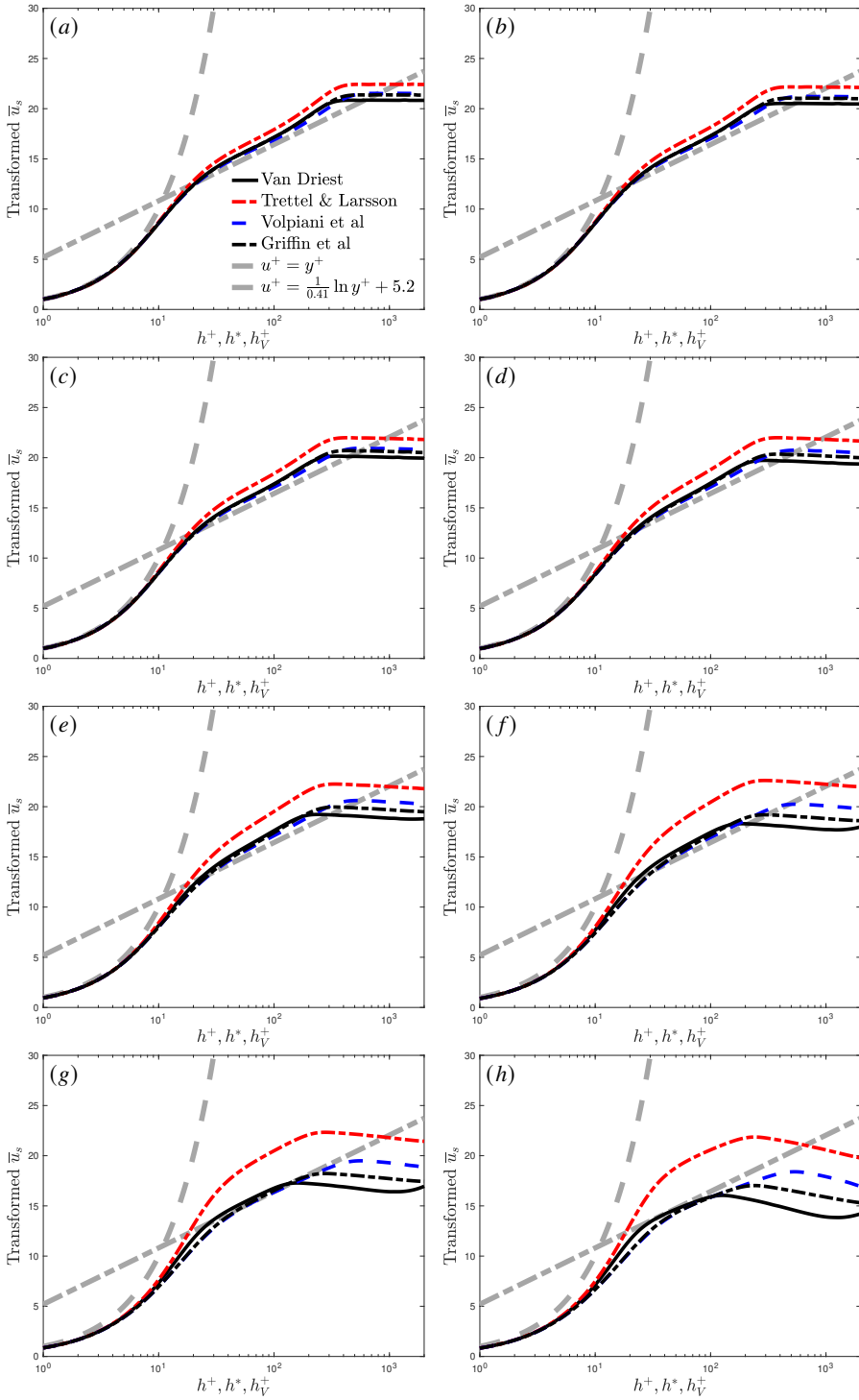


Figure 12: Streamwise mean-velocity profiles, transformed according to several transformations, at different chordwise locations. (a) – (h) stand for the location at chordwise $s_{\mathcal{E}} = 0.00, 4.22, 8.71, 13.50, 18.61, 24.10, 26.99$ and 30.00 , respectively.

layers such as channel flow; however, in the conditions investigated in this study, it inaccurately predicted the logarithmic region. It is well-known that the Van Driest transformation generally performs poorly in compressible, heat-exchanging flat-plate turbulent boundary layer flows. Nevertheless, under the conditions of this study, the Van Driest transformation produced acceptable results. As the position gradually moves away from the attachment line to the point of maximum transverse pressure gradient, different velocity transformations continue to exhibit similar patterns to those observed at the attachment line. This indicates that in the present fully developed three-dimensional turbulent compressible boundary layer, even in the presence of transverse pressure gradients, the mainstream velocity component still largely conforms to the velocity transformations previously established for flat-plate boundary layers. Meanwhile, it is important to note that, under the conditions studied, the transverse velocity components gradually increase from zero along the chordwise direction starting from the attachment line. Therefore, the chordwise velocities at the locations shown in figures (b – d) are not very large. As the transverse velocity increases, shown in figures (e – h), the slopes and intercepts of various transformations for spanwise velocity profiles begin to deviate from the classical relationships. Meanwhile, the transformed streamwise velocity profiles still exhibit a clear log-law region, as shown in figure 12. This indicates that along the streamwise directions, the streamwise mean velocities still exhibit some feature similar to the two-dimensional turbulent boundary layer. When the transverse velocity increases further to a magnitude comparable to the spanwise velocity, the regularity of the entire transformation no longer holds for spanwise velocity. However, the streamwise velocities still show a common behaviour and regions similar to the log-law of the two-dimensional flat-plate boundary layer can also be identified. It should be noted that the results presented here are merely illustrative. Whether a general law-of-the-wall, similar to that in two-dimensional flat-plate boundary layers, exists in three-dimensional boundary layers remains an open question that requires further in-depth investigation.

3.3.2. velocity-temperature relationship

The temperature profiles also play a vital role in compressible boundary, therefore, the widely used relationship between the mean velocity and mean temperature is also shown to assess the scaling relations in three-dimensional boundary layers. The mean temperature-velocity relation model given by Zhang *et al.* (2014), which is also known as the generalized Reynolds analogy, is defined as

$$\left. \begin{aligned} \frac{\bar{T}}{T_e} &= \frac{T_w}{T_e} + \frac{T_{rg} - T_w}{T_e} \frac{\bar{u}_p}{\bar{u}_{p,e}} + \frac{T_e - T_{rg}}{T_e} \left(\frac{\bar{u}_p}{\bar{u}_{p,e}} \right)^2, \\ T_{rg} &= T_e + \frac{r_g \bar{u}_{p,e}^2}{2C_p}, r_g = \frac{2C_p(T_w - \bar{T}_e)}{\bar{u}_{p,e}^2} - 2Pr \frac{\theta_{tw}}{\bar{u}_{p,e} \bar{T}_w} \end{aligned} \right\}, \quad (3.7)$$

where the subscript e stands for the variables at the edge of boundary layer and the velocity \bar{u}_p represents the velocity parallel to the local surface. It should be noted that, in this study, the mean temperature T_e and velocity $\bar{u}_{p,e}$ outside the boundary layer change with the chordwise position s_ξ . The relationship between the mean temperature and mean velocity at different chordwise locations is illustrated in the figure 11. Figure (a) stands for the mean temperature profiles against mean velocity at the exact attachment line $s_\xi = 0$ and the chordwise exit $s_\xi = 30$. It reveals that the relation proposed by Zhang *et al.* (2014) yields an acceptable results. In fact, the accurate prediction results at the exact attachment line are as expected, since it statistically returns to a zero-pressure-gradient flat-plate boundary layer. However, achieving good predictive results at the chordwise exit was surprising. This can be attributed to two potential reasons: in the current flow study, the governing spanwise

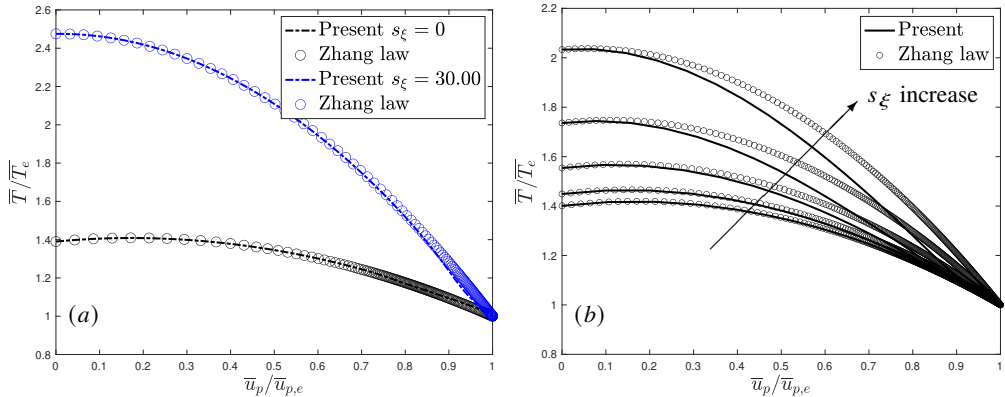


Figure 13: Panels (a) and (b) show the mean temperature profile against mean velocity at several chordwise locations, compared with relation of Zhang *et al.* (2014).

momentum equation for the spanwise velocity w is actually weakly coupled with the other equations, as the boundary layer seems to be homogeneous in spanwise direction. Secondly, at the exit location, although there is a strong crossflow velocity, there is no pressure gradient along either the chordwise or spanwise directions. As a result, the energy generated by the pressure work accumulated upstream is entirely absorbed into the mean flow temperature and velocity.

Then we look at the profiles at the region with both crossflow and pressure gradient effect (figure 13(b)). The figure shows the results from small s_ξ to further chordwise downstream, as pointed by the vector. It can be observed that when the pressure gradient and velocity in the transverse direction are relatively small, the temperature-velocity relationship proposed by Zhang *et al.* (2014) still aligns well with the computational results. As the transverse pressure gradient and transverse velocity increase, the original temperature-velocity relationship begins to deviate in the outer boundary layer region. As the flow further develops downstream, the transverse pressure gradient starts to decrease (figure 6(a)), although the transverse velocity continues to increase. The deviation between the original temperature-velocity relationship and the computational results in the outer boundary layer region gradually diminishes, eventually returning to the trend indicated by the blue line in figure 13(a) at the chordwise exit. These phenomena indicate that the traditional temperature-velocity relationship is significantly influenced by the transverse pressure gradient in three-dimensional boundary layers. Attention must also be given to the observation that, in the chordwise direction downstream from the attachment line, the overall turbulence intensity exhibits a decreasing trend. Additionally, the chordwise velocity in certain regions remains at relatively low levels compared to the spanwise velocity. Therefore, this flow condition might thus differ from typical three-dimensional turbulent boundary layers.

3.4. Reynolds stresses

In this part, we further look at the features of Reynolds stresses of the present simulations. The scaled Reynolds stresses at the exact attachment line are shown in previous and are found in good agreements with the results from incompressible and compressible flat-plate boundary layer. As the transverse pressure gradient begin to increase, the scaled Reynolds stress are shown in figure 14. Two more scaled Reynolds stresses are defined based on the

direction of surface coordinate as follows

$$\left. \begin{aligned} (u_\xi^*)^2 &= \frac{\bar{\rho}}{\bar{\rho}_w} \frac{\overline{u_\xi'' u_\xi''}}{\overline{u_\tau^2}}, \overline{u_\xi'' u_\xi''} = t_x^2 \overline{u'' u''} + t_y^2 \overline{v'' v''} + 2t_x t_y \overline{u'' v''}, \\ (u_n^*)^2 &= \frac{\bar{\rho}}{\bar{\rho}_w} \frac{\overline{u_n'' u_n''}}{\overline{u_\tau^2}}, \overline{u_n'' u_n''} = n_x^2 \overline{u'' u''} + n_y^2 \overline{v'' v''} + 2n_x n_y \overline{u'' v''} \end{aligned} \right\}, \quad (3.8)$$

where $\mathbf{t} = (t_x, t_y)$ and $\mathbf{n} = (n_x, n_y)$ stands for the unit surface tangent and normal vectors, in the $x - y$ plane. From these figures, the evolution of Reynolds stress with chordwise location is clearly presented. When the pressure gradient first affects the turbulence in the attachment line region, there is a slight increase in turbulence intensity, reflected in the slight rise in spanwise Reynolds stress and turbulent kinetic energy (as shown in figures 14(a) and (d)). Subsequently, under the influence of the chordwise favorable pressure gradient, the fluid not only experiences shear in the spanwise direction but also begins to be affected in the chordwise direction. This results in the peak Reynolds stress in the $x - y$ plane shifting towards the wall (figures 14(b, c)). With further acceleration of the fluid in the chordwise direction, chordwise fluctuations become significantly enhanced (figure 14(e)). This indicates that the pressure gradient can, to some extent, induce a redistribution of turbulent energy. However, as the fluid continues to accelerate and develops downstream, fluctuations in all directions show a notable decreasing trend. A noticeable phenomenon is that when the fluctuation intensity shows a significant decrease, the primary Reynolds stress along the chordwise direction exhibits a distribution pattern very similar to that of the primary Reynolds stress in a flat-plate boundary layer (figure 14(e)). Additionally, the fluctuations in the wall-normal direction do not seem to be noticeably affected by the pressure gradient, apart from the last station (figure 14(f)). The variations in general reflect the combined effects of shear caused by the three-dimensional nature of the flow field and the favorable pressure gradient along the chordwise direction.

3.5. Anisotropy tensor

Here, in this section, we try to understand the state of turbulence by using anisotropy tensor of Reynolds stress. The anisotropy tensor \tilde{b}_{ij} , which is defined as

$$\tilde{b}_{ij} = \frac{\overline{\rho u_i'' u_j''}}{\overline{\rho u_i'' u_i''}} - \frac{\delta_{ij}}{3} = \frac{\overline{u_i'' u_j''}}{\overline{u_i'' u_i''}} - \frac{\delta_{ij}}{3} \quad (3.9)$$

is used to understand the state of turbulence at different chordwise location. The invariants of this tensor can be written as (Simonsen & Krogstad 2005)

$$I_1 = \tilde{b}_{ii} = 0, \quad II_2 = -\frac{1}{2} \tilde{b}_{ij} \tilde{b}_{ji}, \quad III_3 = \det(\tilde{b}_{ij}). \quad (3.10)$$

The state of the anisotropy stress tensor can be shown in an anisotropy invariant map, as shown in figure 15. The blue cross stands for the location of the first grid away from the wall surface and the red cross represents the 101th grid away from the surface. All the points, along the wall-normal directions, inside the boundary layer are shown in the figures. The points close to the wall, as $h \rightarrow 0$, are also marked, which are very close to the two-component turbulence, as the wall significantly restricts turbulence fluctuations in the direction normal to the wall in the near-wall region. As the position moves away from the surface, the Reynolds stress anisotropy tensor exhibits a tendency to one-component turbulence. Subsequently, as the position moves further away from the wall, the wall's constraint on the turbulence progressively weakens. The Reynolds stress begins to exhibit characteristics of rod-like turbulence and, with increasing

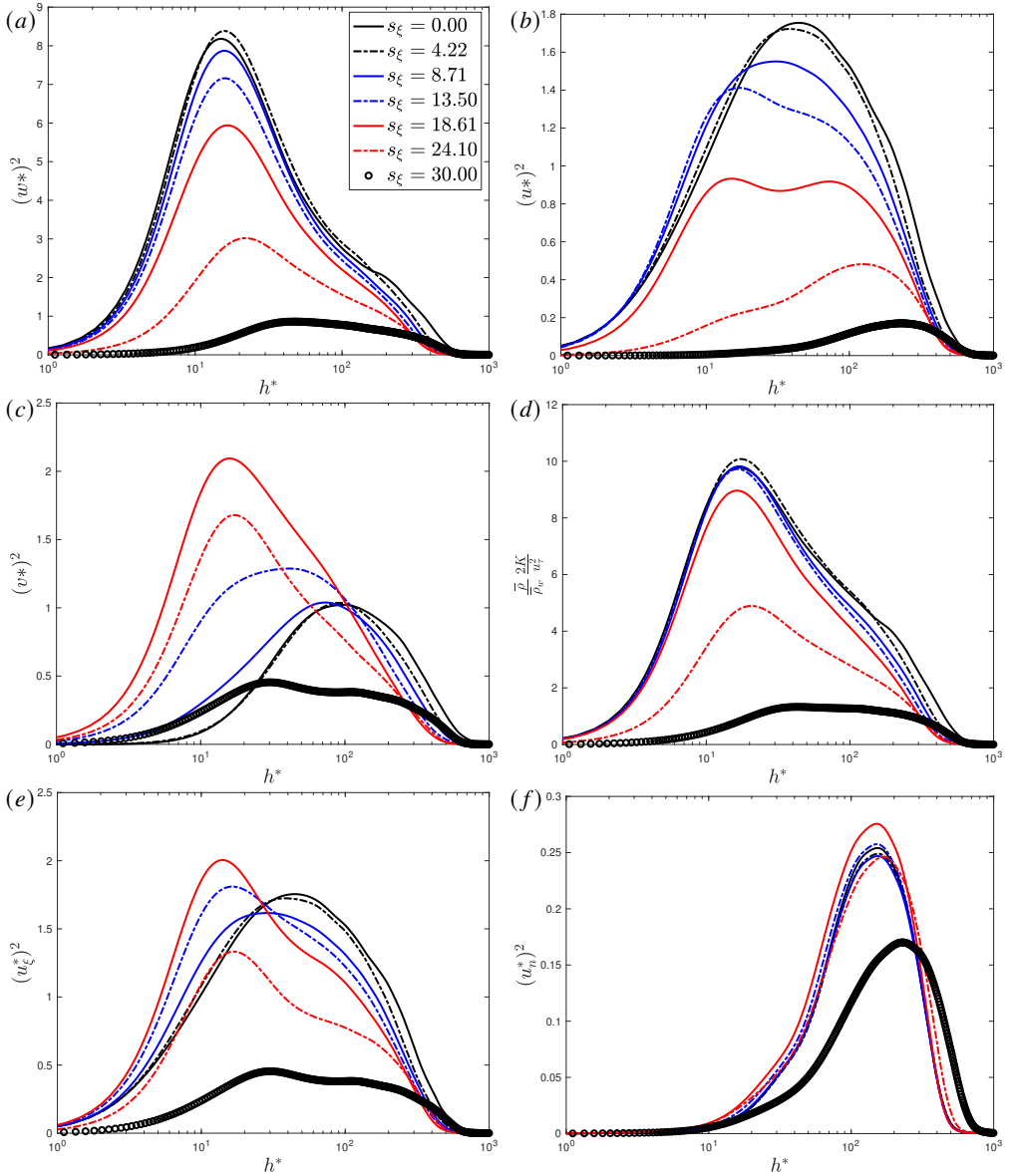


Figure 14: Comparison of the scaled Reynolds stress and kinetic energy at different chordwise locations s_ξ . (a – f) stand for the $(w^*)^2$, $(u^*)^2$, $(v^*)^2$, scaled turbulent kinetic energy $2\bar{\rho}K/(\rho_w u_\tau^2)$, $(u_\xi^*)^2$ and $(u_n^*)^2$, respectively.

distance from the wall, tends to become more isotropic. As the position moves away from the attachment-line boundary layer (from figures 15 (b) to (e)), the distribution characteristics of the anisotropic Reynolds stress tensors remain consistent with those observed at the attachment line. This indicates that the anisotropic characteristics of the Reynolds stress tensors are not significantly affected by the three-dimensional effects, which could provide guidance for subsequent modeling of three-dimensional turbulent boundary layers.

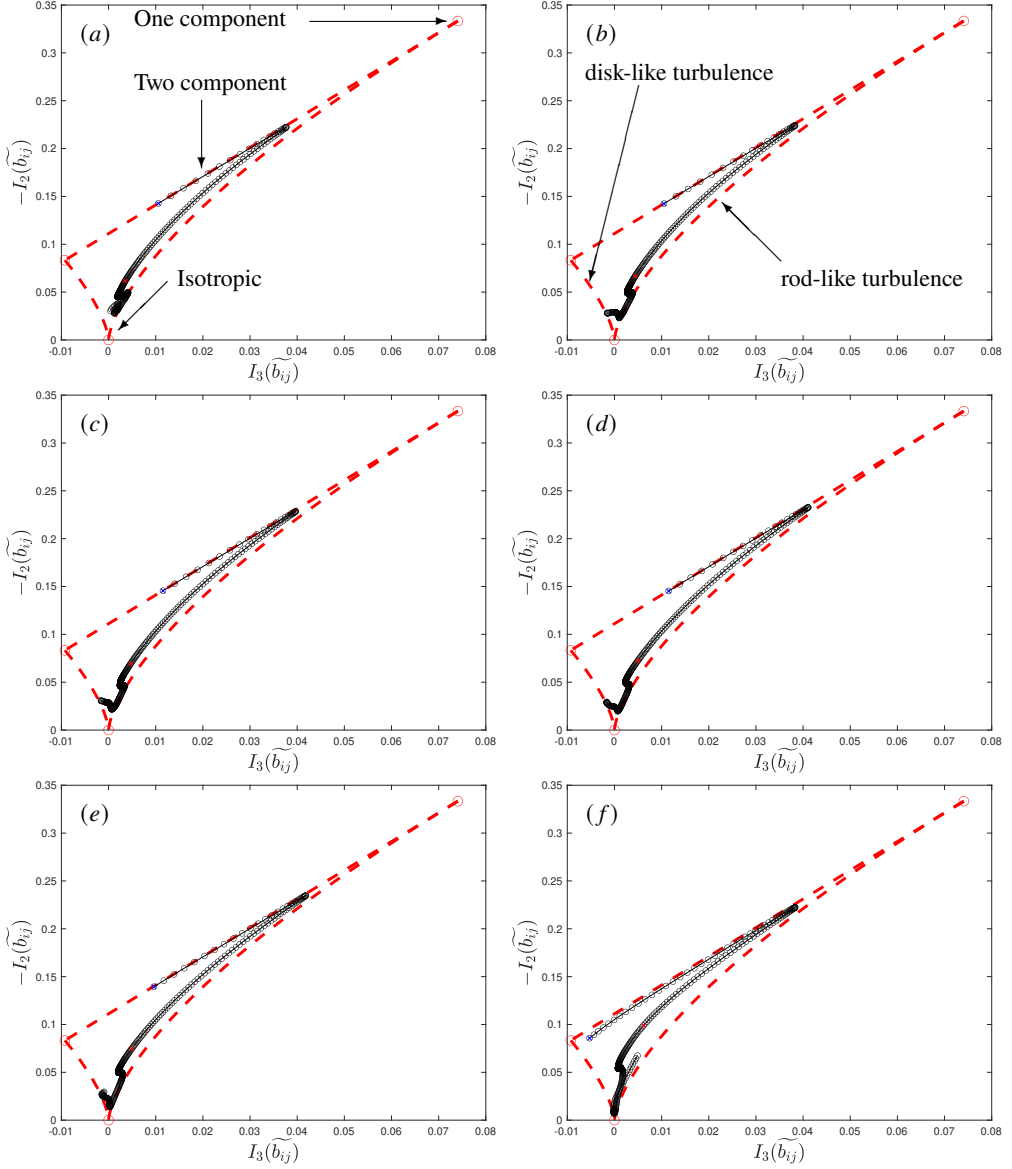


Figure 15: Invariant mapping of Reynolds stress anisotropy in three-dimensional boundary layer at different chordwise locations s_x . (a – f) stand for chordwise locations at $s_x = 0.00, 4.22, 8.71, 13.50, 18.61$ and 30.00 , respectively.

3.6. Turbulent kinetic energy budgets

Further investigation of the turbulence in this three dimensional boundary layer is conducted by analysing the turbulent kinetic energy equation. The transport equation of the turbulent kinetic energy can be expressed as

$$\frac{\partial \bar{\rho}K}{\partial t} = \mathbf{C} + \mathbf{P} + \mathbf{\Pi} + \boldsymbol{\epsilon} + \mathbf{M} + \mathbf{D}, \quad (3.11)$$

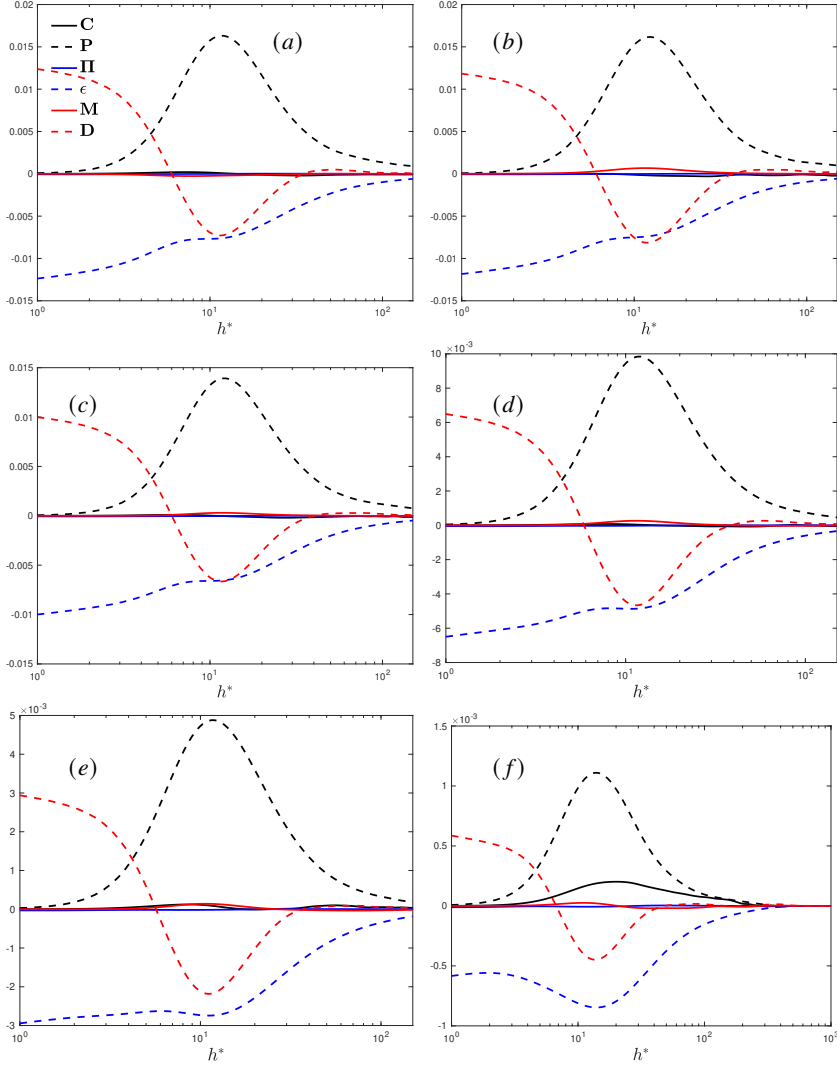


Figure 16: The energy budget distributions along the wall normal direction in three-dimensional boundary layer at different chordwise locations s_ξ . (a – f) stand for chordwise locations at $s_\xi = 0.00, 4.22, 8.71, 13.50, 18.61$ and 24.10 , respectively.

where

$$\left. \begin{aligned}
 \mathbf{C} &= -\frac{\partial \bar{\rho} K \tilde{u}_i}{\partial x_i}, \mathbf{P} = -\bar{\rho} \widetilde{u'_i u'_k} \frac{\partial \tilde{u}_i}{\partial x_k}, \mathbf{\Pi} = \overline{p' \frac{\partial u'_i}{\partial x_i}}, \\
 \boldsymbol{\epsilon} &= -\overline{\tau'_{ik} \frac{\partial u'_i}{\partial x_k}}, \mathbf{M} = \overline{u''_i} \left(\frac{\partial \bar{\sigma}_{ik}}{\partial x_k} - \frac{\partial \bar{p}}{\partial x_i} \right), \\
 \mathbf{D} &= -\frac{\partial}{\partial x_k} \left[\frac{\overline{\rho u''_i u''_i u''_k}}{2} + \overline{p' u'_i} \delta_{ik} - \overline{\tau'_{ik} u'_i} \right],
 \end{aligned} \right\} \quad (3.12)$$

stands for the convection term(**C**), production term(**P**), pressure-dilatation term(**Π**), dissipation rate term(**ϵ**), mass flux term(**M**) and transport-diffusion term(**D**), respectively.

Figure 16 shows the basic results of energy budget distributions along the wall normal direction at several chordwise position. From the distribution shown in the figures 16(a – e), it is evident that the dominant terms are the production term \mathbf{P} , dissipation term ϵ , and the transport-diffusion term \mathbf{D} , consistent with the analysis in traditional two-dimensional boundary layers. This indicates that even though three-dimensional effects significantly alter the flow characteristics (introducing crossflow, pressure gradient effects, etc.), their impact on the turbulence energy balance mechanism is minimal. However, as shown in figure 16(f), the convection term (the black line) become obvious. Although the proportion of the convection term in the energy budget analysis increased, this does not imply an absolute intensification of the convection. In fact, under the influence of the chordwise pressure gradient, the corresponding turbulence is suppressed, leading to a reduction in the production, dissipation and transport-diffusion terms, which in turn makes the convection term more pronounced. This implies that the core modeling terms for turbulence in three-dimensional boundary layer flows remain consistent with those in two-dimensional boundary layers.

3.7. Analysis of Shear Direction Discrepancies

In the previous discussion, we briefly introduced some basic characteristics of the computed three-dimensional turbulent boundary layer. In this section, we will delve deeper into the shear effects within the three-dimensional boundary layer. Traditionally, in two-dimensional turbulent boundary layers (assuming the mainstream and wall-normal velocities are u_ξ and u_n), the focus of shear effects is primarily on $\overline{u'_\xi u'_n}$ and the corresponding meanflow shear du_ξ/dh . However, in three-dimensional cases, the shear effects should actually encompass both $\overline{u'_\xi u'_n}$ and $\overline{w'' u''_n}$, as well as the corresponding du_ξ/dh and dw/dh . From the previous analyses, we observed that the direction of the mean velocity within the boundary layer changes with the distance from the wall. Consequently, the direction of the resultant shear Reynolds stress also varies accordingly. This naturally prompts the question: does the direction of the shear Reynolds stress still align with the direction of the resultant mean flow shear under these conditions?

In general, the Reynolds shear stresses can be expressed as

$$\left. \begin{aligned} \overline{u'_\xi u'_n} &= t_x n_x \overline{u'' u''} + (t_x n_y + t_y n_x) \overline{u'' v''} + t_y n_y \overline{v'' v''}, \\ \overline{w'' u''_n} &= n_x \overline{u'' w''} + n_y \overline{v'' w''} \end{aligned} \right\}, \quad (3.13)$$

and we define the angle $\theta_{rs} = \arctan\left(\overline{w'' u''_n} / \overline{u'_\xi u'_n}\right)$ between the resultant shear Reynolds stress and the chordwise ξ -direction, and the angle $\theta_{ms} = \arctan\left(\overline{\partial w / \partial h} / \overline{\partial u_\xi / \partial h}\right)$ between the mean shear direction and the chordwise direction. The variation of the directional angles of shear Reynolds stress and mean-flow shear at different chordwise locations are shown in figure 17 and some mean-flow velocity components are also shown for better understanding the behaviours.

At different chordwise stations, the distribution of the angles $(\theta_{rs}, \theta_{ms})$ is generally similar and can be divided into three regions along the wall-normal direction. First is the near-wall region, where both θ_{rs} and θ_{ms} exhibit positive angles. There is a significant discrepancy between the two at the wall due to the shear Reynolds stress being zero there, while the mean shear gradient has a substantial value. As the distance from the wall increases, the two angles rapidly converge. In regions with negligible transverse pressure gradients and velocity, θ_{rs} and θ_{ms} approximate equality, indicating a linear relationship between the shear Reynolds stress and the mean flow shear gradient (figure 17(a₁)). As the transverse velocity increases,

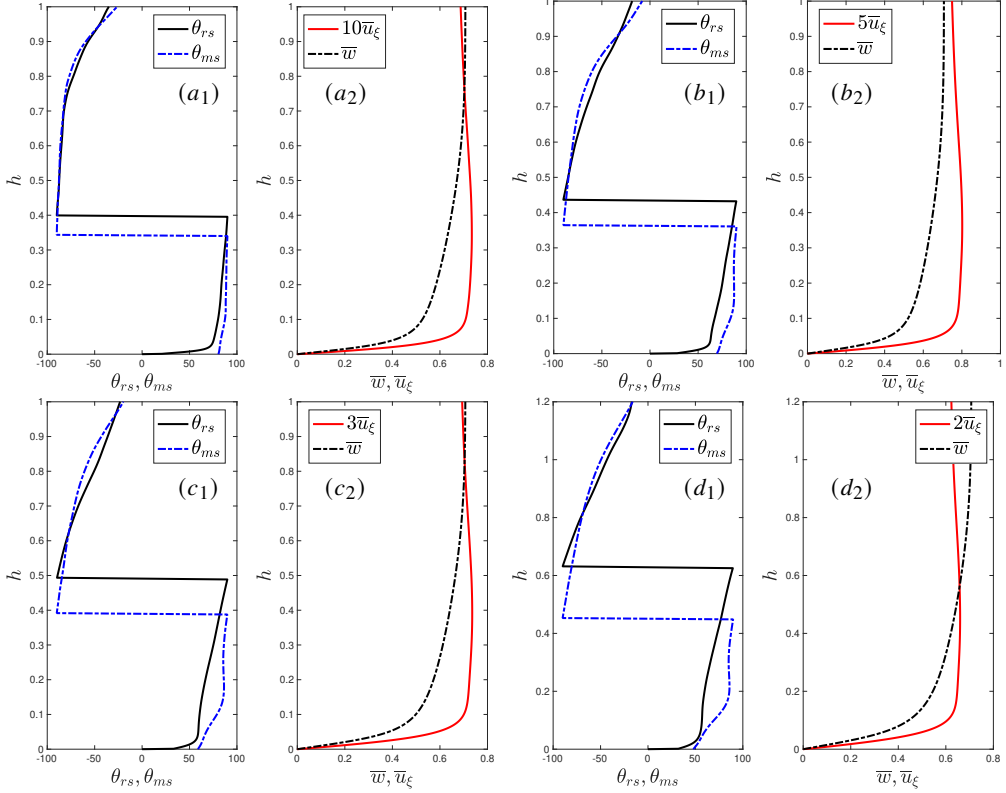


Figure 17: $(a_1 - d_1)$ Variation of the directional angles (θ_{rs} and θ_{ms} in degree) of shear Reynolds stress and mean flow shear with distance from the wall, at several chordwise locations. $(a_2 - d_2)$ The corresponding mean velocity profiles at relative spanwise locations. $(a - d)$ stand for chordwise locations at $s_{\xi} = 4.22, 8.71, 13.50$ and 18.61 , respectively. Some velocity component is enlarged for clarity.

the difference between the two angles in this region also grows, suggesting a nonlinear relationship between the Reynolds shear stress and the mean flow shear when the transverse components (\bar{u}_{ξ} in figures 17($a_2 - d_2$)) become sufficiently large (figures 17($b_1 - d_1$)). When the wall-normal distance further increases, a sudden change in the angles is observed. This is attributable to the pressure gradient causing the velocity profile to overshoot, resulting in a reversal of the mean flow gradient from positive to negative. A similar phenomenon occurs in the shear Reynolds stress, but its change lags behind the mean flow shear, with the extent of this lag increasing with higher transverse velocities. After these angular transitions, both θ_{rs} and θ_{ms} quickly return to similar levels, indicating that in the outer region of the boundary layer, at a certain distance from the wall, the shear Reynolds stress and mean flow shear again appear to exhibit a linear relationship. This observation indicates that, in the case of three-dimensional flows, the relationship between the shear Reynolds stress and the mean flow shear is inherently nonlinear. Consequently, a simple linear approximation would introduce certain inaccuracies.

4. Conclusions

Overall, this study represents the second part of our series on hypersonic swept blunt-body flows. In this segment, we have examined the characteristics of three-dimensional turbulent

boundary layers in the presence of transverse flow and pressure gradients. The main findings of this study are as follows:

- In the flow over a swept blunt body discussed in this paper, even without the assumption of infinite sweep, if the boundary layer reaches a fully developed turbulent state, the subsequent flow state also satisfies the infinite sweep assumption—the boundary layer is homogeneous along the spanwise direction.

- We examined the law-of-the-wall and the temperature-velocity relationship, which have been widely applied in two-dimensional turbulent boundary layers, within the context of three-dimensional boundary layers. Our findings indicate that, when the transverse velocity is not excessively high, the spanwise velocity still adheres to some classical velocity transformation relationships. Excluding the Trettel & Larrson transformation, existing transformation forms generally yield good predictive results, with the transformations proposed by Griffin *et al.* (2021) and Volpiani *et al.* (2020) aligning best with incompressible scaling. However, as the transverse velocity further increases, the spanwise velocity no longer conforms to traditional scaling laws. Instead, the streamwise velocity u_s , in the present condition, conforms to traditional scaling laws and classical transformations can collapse the data to the log-law of the incompressible ones. We further examined the applicability of the temperature-velocity relationship proposed by Zhang *et al.* (2014) under such three-dimensional conditions. The study found that, in the absence of pressure gradients or when the transverse velocity is relatively low, the traditional temperature-velocity relationship still holds well. However, when the pressure gradient and transverse velocity are significant, the predictive accuracy of the temperature-velocity relationship markedly diminishes. The potential reason for this deviation is that in boundary layers with pressure gradients, the velocity profile along the direction of the pressure gradient exhibits an overshoot, which significantly alters the corresponding relationship between temperature and velocity, leading to an overestimation in the predictive results.

- Analysis of fluctuating velocities, temperature, Reynolds stresses, Reynolds stress anisotropy tensors, and turbulent kinetic energy in three-dimensional boundary layers indicates that the fundamental turbulent characteristics remain qualitatively consistent with those in two-dimensional turbulent boundary layers. Typical near-wall streak structures still appear in three-dimensional turbulent boundary layers and correspond with the energetic structures in the outer region. However, due to the three-dimensional effects, turbulent energy is redistributed within the three-dimensional turbulent boundary layer. This redistribution causes the turbulent energy to align more with the three-dimensional mean flow direction, resulting in the streak structures tending to orient along the direction of the external streamlines.

- By analyzing and comparing the directions of the shear Reynolds stress and the mean flow shear, the study found that in the near-wall region, when the transverse flow velocity is relatively low, the two align well. However, when the transverse velocity is high, there is a significant deviation between their directions. Additionally, with the introduction of a pressure gradient in the transverse direction, the velocity profile in the corresponding direction exhibits an overshoot, which alters the mean flow shear direction. The shear Reynolds stress also undergoes a similar change, but with a certain lag, and this lag increases with higher transverse velocity. Finally, in the outer region, some distance away from the wall, the directions of the shear Reynolds stress and mean flow shear are essentially consistent. This indicates that in three-dimensional boundary layers with transverse flow, the relationship between shear Reynolds stress and mean flow shear is partitioned: it is nonlinear in the inner region and can be approximated to return to a linear relationship in the outer region.

Finally, we would like to say that the leading edge of the swept configuration is an ideal model for studying three-dimensional turbulent boundary layers. It effectively bridges the

traditional, unified concepts of two-dimensional turbulent boundary layers with the unique effects inherent to three-dimensional turbulent boundary layers.

Supplementary data.

Acknowledgements. We acknowledge Yancheng MetaStone Tech. Co. for providing us with all the computational resources required by this work. Useful discussions with Professor Chunxiao Xu, Professor Qibing Li of Tsinghua University, Professor Jie Ren of Beijing Institute of Technology, Dr. Jian Liu of China Aerodynamics Research and Development Center and Dr. Yi Huang of China Academy of Launch Vehicle Technology are gratefully acknowledged.

Funding. This work received support from the NSFC Grants 12202242, 12172195 and 12388101. The authors are also grateful for the support from the National Key Research and Development Plan of China through project no. 2019YFA0405201 and the National Key Project GJXM92579 and the Grants 20231001 in Supercomputing Center in Yancheng.

Declaration of interests. The authors report no conflict of interest.

Data availability statement. The full data set of the simulations is of the order of thousands of gigabytes. By contacting the authors, a smaller subset can be made available.

Author ORCIDs.

Youcheng Xi, <https://orcid.org/0000-0002-6484-0231>;
Bowen Yan, <https://orcid.org/0009-0002-0655-9414>;
Guangwen Yang, <https://orcid.org/0000-0002-8673-8254>
Song Fu, <https://orcid.org/0000-0003-2052-7435>

Author contributions. Youcheng Xi: Funding acquisition, Conceptualization, Data curation, Formal analysis, Coding, Investigation, Methodology, Validation, Writing original draft. Bowen Yan & Guangwen YANG: Software and optimization on high performance computing, Computational Resources. Song Fu: Funding acquisition, Supervision, Resources, Writing-review & editing.

REFERENCES

- COGO, MICHELE, SALVADORE, FRANCESCO, PICANO, FRANCESCO & BERNARDINI, MATTEO 2022 Direct numerical simulation of supersonic and hypersonic turbulent boundary layers at moderate-high reynolds numbers and isothermal wall condition. *Journal of Fluid Mechanics* **945**, A30.
- DONG, SIWEI, YU, MING, TONG, FULIN, WANG, QIAN & YUAN, XIANXU 2024 Hypersonic turbulent boundary layer over the windward side of a lifting body. *Journal of Fluid Mechanics* **988**, A29.
- DUAN, L., BEEKMAN, I. & MARTÍN, M. P. 2010 Direct numerical simulation of hypersonic turbulent boundary layers. part 2. effect of wall temperature. *Journal of Fluid Mechanics* **655**, 419–445.
- DUAN, L., BEEKMAN, I. & MARTÍN, M. P. 2011 Direct numerical simulation of hypersonic turbulent boundary layers. part 3. effect of mach number. *Journal of Fluid Mechanics* **672**, 245–267.
- DUAN, LIAN, CHOUDHARI, MEELAN M & WU, MINWEI 2014 Numerical study of acoustic radiation due to a supersonic turbulent boundary layer. *Journal of Fluid Mechanics* **746**, 165–192.
- GAITONDE, DATTA V. & ADLER, MICHAEL C. 2023 Dynamics of three-dimensional shock-wave/boundary-layer interactions. *Annual Review of Fluid Mechanics* **55** (1), 291–321.
- GANAPATHISUBRAMANI, B., CLEMENS, N. T. & DOLLING, D. S. 2006 Large-scale motions in a supersonic turbulent boundary layer. *Journal of Fluid Mechanics* **556**, 271–282.
- GATSKI, THOMAS B. & BONNET, JEAN-PAUL 2013 *Compressibility, Turbulence and High Speed Flow*, 2nd edn. UK: Academic Press.
- GRIFFIN, KEVIN PATRICK, FU, LIN & MOIN, PARVIZ 2021 Velocity transformation for compressible wall-bounded turbulent flows with and without heat transfer. *Proceedings of the National Academy of Sciences* **118** (34), e2111144118.
- HUANG, P. G., COLEMAN, G. N. & BRADSHAW, P. 1995 Compressible turbulent channel flows: Dns results and modelling. *Journal of Fluid Mechanics* **305**, 185–218.
- HUTCHINS, N. & MARUSIC, IVAN 2007 Evidence of very long meandering features in the logarithmic region of turbulent boundary layers. *Journal of Fluid Mechanics* **579**, 1–28.
- JIMÉNEZ, JAVIER, HOYAS, SERGIO, SIMENS, MARK P. & MIZUNO, YOSHINORI 2010 Turbulent boundary layers and channels at moderate reynolds numbers. *Journal of Fluid Mechanics* **657**, 335–360.

- KONRAD, WOLFGANG & SMITS, ALEXANDER J. 1998 Turbulence measurements in a three-dimensional boundary layer in supersonic flow. *Journal of Fluid Mechanics* **372**, 1–23.
- MORKOVIN, M. V. 1962 Effects of compressibility on turbulent flows. In *Mecanique de la Turbulence* (ed. A. Favre) p. 367–380.
- PIROZZOLI, SERGIO & BERNARDINI, MATTEO 2011 Turbulence in supersonic boundary layers at moderate reynolds number. *Journal of Fluid Mechanics* **688**, 120–168.
- SIMONSEN, A. J. & KROGSTAD, P.-Å. 2005 Turbulent stress invariant analysis: Clarification of existing terminology. *Physics of Fluids* **17** (8), 088103.
- SMITH, M. W. & SMITS, A. J. 1995 Visualization of the structure of supersonic turbulent boundary layers. *Experiments in Fluids* **18** (4), 288–302.
- SMITS, A. J. & DUSSAUGE, J.-P. 2005 *Turbulent Shear Layers in Supersonic Flow*, 2nd edn. New York, NY 10013, USA: Springer New York, NY.
- TRETTEL, ANDREW & LARSSON, JOHAN 2016 Mean velocity scaling for compressible wall turbulence with heat transfer. *Physics of Fluids* **28** (2), 026102.
- VAN DRIEST, E. R. 1951 Turbulent boundary layer in compressible fluids. *Journal of the Aeronautical Sciences* **18** (3), 145–160.
- VOLPIANI, PEDRO S., IYER, PRAHLADH S., PIROZZOLI, SERGIO & LARSSON, JOHAN 2020 Data-driven compressibility transformation for turbulent wall layers. *Physical Review Fluids* **5** (5), 052602.
- ZHANG, YOU-SHENG, BI, WEI-TAO, HUSSAIN, FAZLE & SHE, ZHEN-SU 2014 A generalized reynolds analogy for compressible wall-bounded turbulent flows. *Journal of Fluid Mechanics* **739**, 392–420.